Electronic structure of the kagome compound $CaTi_3Bi_4$ using high-field torque magnetometry and density functional theory

Kyryl Shtefiienko,[1,*] Cole Phillips,[1,*] Brenden R. Ortiz,[2] David E. Graf,[3,4] and Keshav Shrestha[1,†]

[1]*Department of Chemistry and Physics, West Texas A&M University, Canyon, Texas 79016, USA*

[2]*Materials Science and Technology Division, Oak Ridge National Laboratory, Oak Ridge, Tennessee 37831, USA*

[3]*Department of Physics, Florida State University, Tallahassee, Florida 32306, USA*

[4]*National High Magnetic Field Laboratory, Tallahassee, Florida 32310, USA*

(Received 4 September 2025; revised 22 November 2025; accepted 17 December 2025; published 16 January 2026)

We report systematic torque magnetometry measurements to investigate the electronic properties of the newly discovered kagome compound $CaTi_3Bi_4$. Electrical transport, magnetic susceptibility, and thermal measurements reveal no evidence of a magnetic ground state in this material. Torque data obtained in magnetic fields up to 41.5 T exhibit clear de Haas–van Alphen (dHvA) oscillations, with nine distinct frequencies ranging from 13 to 6164 T. Angular-dependent dHvA measurements show that, with the exception of the lowest frequency (13 T), all observed frequencies nearly follow a $1/\cos\theta$ dependence, where θ is the angle between the crystallographic c axis and the magnetic field direction. This behavior is characteristic of quasi-two-dimensional Fermi-surface sheets with nearly circular cross sections. To further elucidate the electronic structure, we performed density functional theory (DFT) calculations of the band structure and Fermi surface. The calculated bands reveal the presence of multiple Dirac points (DP), flat bands (FB), and van Hove singularities (VHS) near the Fermi level. The resulting Fermi surface consists of several quasi-two-dimensional cylindrical sheets, consistent with the experimentally observed $1/\cos\theta$ dependence. Notably, the theoretical dHvA frequencies, derived from extremal Fermi-surface cross-sectional areas, agree well with the experimental values and reproduce their angular dependence. Remarkably, all experimentally observed frequencies are captured by the DFT predictions. Pressure-dependent calculations up to 10 GPa show that the electronic features—DP, FB, and VHS—evolve systematically with pressure. In particular, the VHS shifts closer to the Fermi level, demonstrating that pressure acts as an effective tuning parameter in this material. These combined experimental and theoretical results provide a comprehensive understanding of the electronic structure of $CaTi_3Bi_4$ and demonstrate how pressure can be used to tune its key electronic features, offering valuable guidance for exploring related kagome materials.

DOI: 10.1103/5fp5-xd6m

I. INTRODUCTION

Newly discovered kagome materials have attracted considerable research interest as they provide a platform for a variety of intriguing physical phenomena, including charge density wave (CDW), superconductivity, frustrated magnetism, and more [1–3]. These compounds feature a corner-sharing triangular lattice and hexagon structure reminiscent of traditional Japanese basket weaving [4]. A prominent example is the vanadium-based AV_3Sb_5 family (A = K, Rb, Cs), also referred to as the 135 family, which consists of a hexagonal lattice of V atoms coordinated by Sb atoms [5–7]. This family hosts a range of exotic quantum states, such as superconductivity with critical temperatures (T_c) between 0.9 and 2.5 K and CDW order near $T^* \sim 90$–105 K [8–12]. Density functional theory (DFT) studies have shown that this family possesses flat bands as well as multiple Dirac and van Hove singularity points, and these features are located near the Fermi level. Furthermore, the nontrivial topology of AV_3Sb_5 has been confirmed through $\mathbb{Z}_2$ invariant calculations using DFT [7,13] and Berry phase estimations from quantum oscillation measurements [14–24].

A newly discovered family of Ti-based kagome compounds, $RETi_3Bi_4$ (RE = rare earth) [25,26], commonly referred to as the 134 family, crystallizes in an orthorhombic structure with space group $Fmmm$ (No. 69). The unit cell hosts four kagome layers formed by the Ti sublattice, as shown in Fig. 1. These compounds feature slightly distorted kagome networks together with zigzag RE chains embedded within RE Bi bilayers. The localized $4f$ magnetism of the lanthanide ions makes this family particularly appealing, as it provides a platform to explore magnetically tuned exotic phases in kagome systems.

DFT and angle-resolved photoemission spectroscopy studies [27–33] have revealed van Hove singularities and Dirac points near the Fermi level in these materials. L. Chen *et al.* [34] carried out *in situ* resistance measurements in $NdTi_3Bi_4$ under high pressure and found that the ferromagnetic ordering temperature changes with pressure, demonstrating the tunability of $RETi_3Bi_4$ under external pressure. Recently, single-crystal neutron diffraction combined with DFT studies in $CeTi_3Bi_4$ [35] exhibits an unusual spin-density-wave-like ground state, driven by the interaction between the Ce

*These authors contributed equally to this work.

†Contact author: kshrestha@wtamu.edu

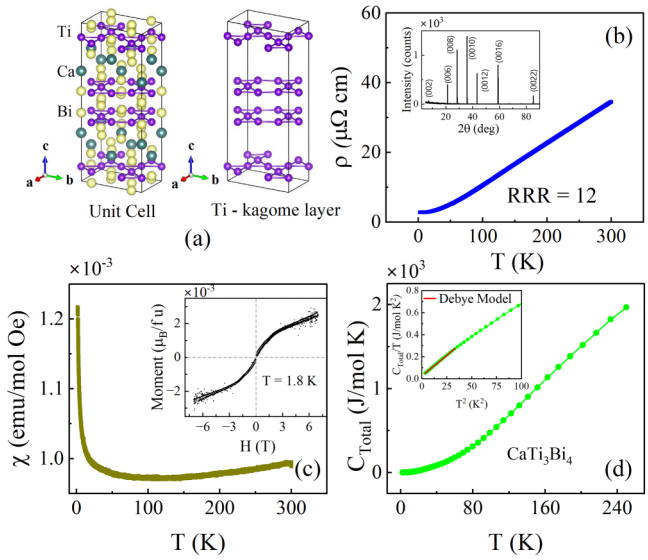

FIG. 1. (a) Crystal structure of $CaTi_3Bi_4$ showing the full unit cell (left) and the kagome layer of Ti atoms (right). (b) Temperature dependence of electrical resistance, $R(T)$, showing metallic behavior with a residual resistance ratio (RRR) of 12. Inset: The x-ray diffraction pattern showing only (00L) reflections, confirming c axis orientation and high crystallinity. (c) Magnetic susceptibility, $\chi(T)$, as a function of temperature, indicating typical paramagnetic behavior. (d) Heat capacity as a function of temperature. Inset: Field-dependent magnetic moment measured at 1.8 K. The moment varies linearly with magnetic field without hysteresis, confirming the absence of any intrinsic magnetic ordering. Together, the electrical, magnetic, and thermal measurements confirm a nonmagnetic ground state. Inset: Debye model fit (red curve) to the heat capacity data.

magnetic sublattice and the Ti kagome electronic structure. However, studies on the Fermi surface of $RETi_3Bi_4$, particularly via quantum oscillation measurements, remain limited. We recently conducted torque measurements [36] in one of the family members, $YbTi_3Bi_4$, and observed a forward-leaning, sawtoothlike waveform in the de Haas–van Alphen (dHvA) effect. By performing both angle- and temperature-dependent torque measurements along with DFT calculations, we mapped the Fermi surface of $YbTi_3Bi_4$.

Here we report the electronic structure of $CaTi_3Bi_4$ via dHvA oscillations and first-principles calculations. Notably, $CaTi_3Bi_4$ is the only member of the ATi_3Bi_4 (A = alkaline-earth) family that does not contain a rare-earth element. While its synthesis, crystal structure, electrical transport, and density of states have been previously reported [37], the detailed electronic structure—particularly the band dispersion and Fermi surface—remains unexplored. In this work, we performed high-field torque magnetometry measurements together with DFT calculations. Torque measurements up to 41.5 T reveal pronounced dHvA oscillations with nine distinct frequency components. The band structure exhibits flat bands, Dirac points, and a van Hove singularity near the Fermi level, while the Fermi surface features multiple quasi-two-dimensional, cylindrical-like sheets. We show that the calculated extremal cross sections of the Fermi surface yield frequencies in good agreement with the experimental observations.

TABLE I. Average elemental composition of $CaTi_3Bi_4$ single crystals obtained from EDS measurements over multiple spots. The measured values are close to the nominal composition (Ca:Ti:Bi = 12.5:37.5:50.0) within experimental uncertainty.

Element	Atomic (%)	Std. dev. (±%)
Ca	11.9	1.1
Ti	38.5	1.0
Bi	49.6	1.2

II. EXPERIMENTAL AND COMPUTATIONAL DETAILS

Single crystals of $CaTi_3Bi_4$ were synthesized using a Bi self-flux method. Elemental dendritic Ca (99.9%, Alfa), Ti powder (99.99%, Alfa), and Bi shot (99.999%) were combined in a 2:3:10 molar ratio and placed into 2-ml Canfield crucibles equipped with a catch crucible and a porous frit [38]. The crucibles were sealed under 0.7 atm of argon gas in fused silica ampoules. The samples were heated to 1000 °C at a rate of 200 °C/h, held at 1000 °C for 18 h to homogenize, and then cooled to 600 °C at a rate of 1–2 °C/h. After dwelling at 600 °C for 4 h, the ampoules were centrifuged to remove excess Bi. The resulting crystals are large (1–5 mm), pseudohexagonal plates with a metallic silver luster. They are soft and can be easily exfoliated along the (00L) plane using adhesive tape.

The x-ray diffraction pattern of a $CaTi_3Bi_4$ single crystal using a powder diffractometer is shown in Fig. 1(b) inset. The presence of a series of sharp (00L) reflections confirm that the crystal surface is oriented along the c axis. The absence of additional peaks indicates high crystallinity and phase purity. The composition of the $CaTi_3Bi_4$ single crystals was examined using energy-dispersive x-ray spectroscopy (EDS). The averaged results (Table I) confirm a near-stoichiometric composition (Ca: 11.9%, Ti: 38.5%, Bi: 49.6%), consistent with the nominal $CaTi_3Bi_4$ ratio within the uncertainty of the measurement. The crystals are moderately reactive to air and water, exhibiting visible tarnishing within a few hours in ambient conditions.

Electrical transport, magnetic susceptibility, and heat capacity measurements were performed using a PPMS (Quantum Design). The electrical resistance was measured by using a standard four-probe contact method with the applied current of 2.5 mA. Torque measurements were carried out using a miniature piezoresistive cantilever to detect dHvA oscillations. A selected $CaTi_3Bi_4$ single crystal was mounted on the cantilever arm using vacuum grease and then attached to a rotating platform. The probe was slowly cooled to a base temperature of 0.5 K. Two resistive elements on the cantilever, along with two room-temperature resistors, formed a Wheatstone bridge, which was balanced at base temperature before sweeping the magnetic field. The sample was rotated *in situ* under applied magnetic fields at various tilt angles (θ), where θ is defined as the angle between the magnetic field and the crystallographic c axis [see inset of Fig. 2(a)]. Magnetic fields were swept at each fixed temperature at a rate of 1.5 T/min.

The first-principles calculations were performed using the QUANTUM ESPRESSO package [39] based on DFT [40,41]. The exchange–correlation effects were treated within the

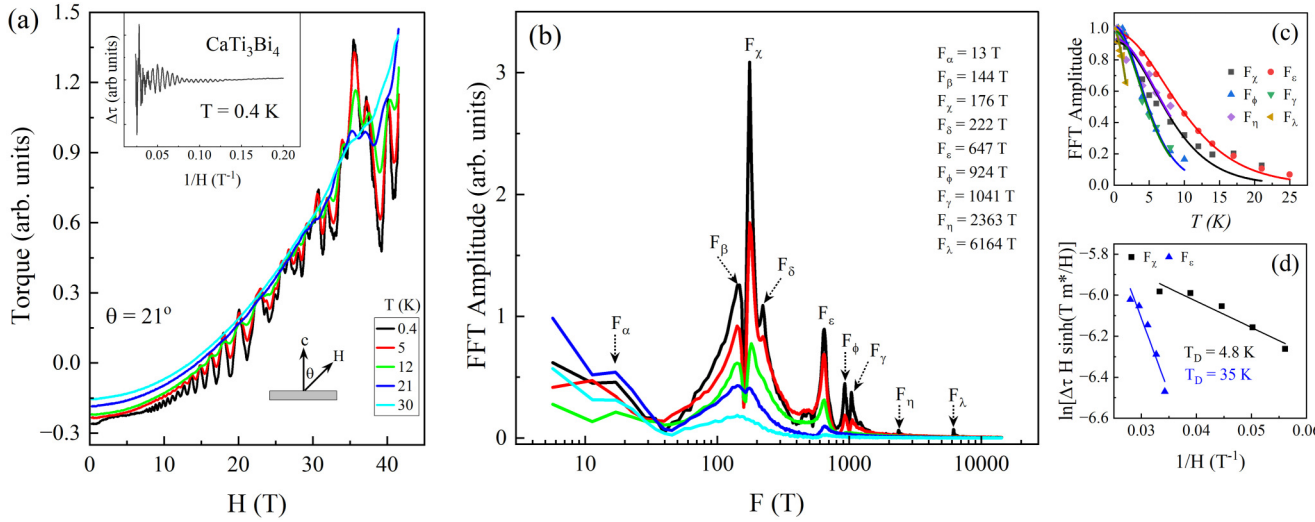

FIG. 2. (a) Magnetic torque τ measured on a $CaTi_3Bi_4$ single crystal in fields up to 41.5 T at $T = 0.5$ K and tilt angle $\theta = 21°$. Clear dHvA oscillations are observed, which weaken with increasing temperature. Lower inset: Definition of the tilt angle θ. Upper inset: Background-subtracted torque signal at $T = 0.4$ K. (b) Fast Fourier transform (FFT) of the dHvA oscillations in (a), revealing eight distinct frequencies ranging from 144 to 6164 T. The x axis is shown on a logarithmic scale for better visibility of the frequency peaks. (c) Temperature dependence of the FFT amplitude (symbols) and best fits using the Lifshitz-Kosevich (LK) formula (2) (solid curves). (d) Dingle temperature T_D analysis for two frequencies, F_χ and F_ϵ.

generalized gradient approximation using the Perdew-Burke-Ernzerhof functional revised for solids, which provides an improved description of equilibrium lattice parameters in crystalline materials [42]. Ultrasoft pseudopotentials from the standard QUANTUM ESPRESSO pseudopotential library were employed for Bi, Ca, and Ti atoms. The plane-wave kinetic energy and charge-density cutoffs were set to 70 and 560 Ry, respectively. The Brillouin zone was sampled using a Γ-centered Monkhorst-Pack k-point mesh of $8 \times 8 \times 5$ for the self-consistent field calculations, chosen to reflect the anisotropic lattice parameters and to ensure convergence of the total energy and charge density. We verified that further increasing the k-point density does not lead to noticeable changes in the band dispersion near the Fermi level.

For Fermi-surface mapping, eigenvalues were computed in a non-self-consistent calculation on a much denser $20 \times 20 \times 20$ k -point grid to achieve sufficient resolution of the Fermi-surface topology. Spin-orbit coupling (SOC) was included self-consistently in the electronic structure calculations using fully relativistic pseudopotentials, with particular importance for the Bi atoms due to their strong relativistic effects. Theoretical quantum oscillation frequencies were obtained from the calculated Fermi surfaces using the SKEAF code [43], using the self-consistent DFT Fermi level without applying any rigid Fermi-level shift.

III. RESULTS AND DISCUSSION

Figure 1 presents the electrical transport, magnetic susceptibility, and heat capacity measurements of $CaTi_3Bi_4$ over a temperature range from 300 K to 2.5 K. The electrical resistance $R(T)$, shown in Fig. 1(b), decreases monotonically with decreasing temperature, confirming the metallic nature of the material. The residual resistance ratio (RRR), defined as $R(300\ \text{K})/R(2.5\ \text{K})$, is found to be 12, which is higher than the previously reported value of 8 [37], indicating improved crystal quality in this work. The magnetic susceptibility $\chi(T)$ exhibits a typical paramagnetic response across the entire temperature range [Fig. 1(c)]. The $\chi(T)$ shows a weak, nearly temperature-independent behavior, consistent with a nonmagnetic ground state. The small upturn at low temperature is attributed to trace paramagnetic impurities. No anomalies indicative of magnetic or structural transitions were observed. The magnetic moment versus H plot at 2 K (inset) shows a linear, nonhysteretic behavior, further confirming the absence of intrinsic magnetism.

The temperature dependence of the total heat capacity $C_{\text{Tot}}(T)$ is shown in Fig. 1(d). Heat capacity was measured between 2 K and 240 K; measurements were not extended to 300 K because the N-grease used for thermal contact in our setup is not reliable above ∼200 K, and acquiring reliable data to 300 K would require remounting with a different contact medium and a separate dataset. According to the Debye model [44–46], the total heat capacity of a metal can be expressed as the sum of electronic and phononic contributions,

$$C_{\text{Tot}} = C_{\text{El}} + C_{\text{Ph}} = \gamma T + \beta T^3. \quad (1)$$

Here γ and β are fitting parameters. The coefficient γ, referred to as the Sommerfeld coefficient, is directly proportional to the electronic density of states at the Fermi level. The phononic term β is related to the Debye temperature Θ_D. The inset of Fig. 1(d) shows the fit of the heat-capacity data using the Debye model [Eq. (1)]. From this fit, the parameters are obtained as $\gamma = 25.86\ \text{mJ mol}^{-1}\ \text{K}^{-2}$ and $\beta = 0.67\ \text{mJ mol}^{-1}\ \text{K}^{-4}$. These values, particularly γ, are comparable to those of the sister compound $YbTi_3Bi_4$ [28,34]. From the β value, the Debye temperature Θ_D is estimated to be 285 K for $CaTi_3Bi_4$.

Here all these electrical, magnetic, and thermal measurements confirm that $CaTi_3Bi_4$ is a good metal and

show no evidence of magnetic ordering, charge-density-wave formation, or superconducting transitions from 300 K down to 2.5 K. To investigate the electronic structure of $CaTi_3Bi_4$, we performed magnetic torque (τ) measurements in applied fields up to 41.5 T.

Figure 2(a) shows the field dependence of the torque, $\tau(H)$, at selected temperatures. The measurements were conducted at a tilt angle of 21° between the magnetic field and the crystallographic c axis, as illustrated in the inset. Clear dHvA oscillations are observed above moderate magnetic fields of 5 T. The oscillations are pronounced at low temperatures and gradually diminish at higher temperatures due to thermal damping. Looking into the oscillations, there appear to be more than one period, indicating the presence of multiple frequencies in the oscillations. To extract the frequencies, we first subtracted a smooth polynomial background and performed a fast Fourier transform (FFT). The background-subtracted data are shown in the upper inset. As shown in Fig. 2(b), the frequency spectrum of dHvA oscillations shows rich features with the presence of eight distinct frequency peaks, located at $F_\alpha = 13$, $F_\beta = 144$, $F_\chi = 176$, $F_\delta = 222$, $F_\epsilon = 647$, $F_\phi = 924$, $F_\gamma = 1041$, $F_\eta = 2363$, and $F_\lambda = 6164$ T. Among these peaks, F_χ is the dominant one, with an amplitude nearly three times higher than the others. This peak shows robust presence at high temperatures and higher tilt angles. It is important to note that a low-frequency peak near 0–10 T usually appears in the frequency spectrum due to improper background subtraction. However, our DFT calculations also show the presence of a small frequency in the range of 20–25 T, indicating that F_α is an intrinsic feature.

The decreasing trend of the dHvA oscillation amplitude with temperature can be explained by the Lifshitz-Kosevich (LK) theory [47,48]. According to the LK theory, the oscillatory component of the torque varies with temperature and magnetic field as

$$\Delta\tau(T,H) \propto e^{-\lambda_D} \frac{\lambda(T/H)}{\sinh[\lambda(T/H)]}, \tag{2}$$

where $\lambda_D(H) = \frac{2\pi^2 k_B}{\hbar e} m^* \frac{T_D}{H}$ and $\lambda(T/H) = \frac{2\pi^2 k_B}{\hbar e} m^* \frac{T}{H}$. Here T_D denotes the Dingle temperature, while $\hbar$ and k_B are the reduced Planck constant and Boltzmann constant, respectively. The exponential term, known as the Dingle factor, accounts for the damping of oscillations with decreasing magnetic field. The thermal damping factor, represented by the $\sinh^{-1}$ term, describes the suppression of oscillation amplitude at elevated temperatures. Therefore, by fitting the temperature dependence of the dHvA oscillations, we can estimate the effective mass of charge carriers.

We performed LK analyses on the major frequency peaks, including the high-frequency components F_η and F_λ. The high-frequency signals are weak and highly sensitive to temperature, making them difficult to resolve above 5 K. Therefore, in order to perform LK analysis of these high-frequency signals, we collected sufficient data points between 0.4–5 K. The inset of Fig. 2(b) presents the amplitude of the frequency peaks at different temperatures. As expected, the amplitude decreases at higher temperatures. We have plotted the amplitude as a function of temperature for dominant peaks, as shown in Fig. 2(c). The scattered symbols represent the experimental data, while the solid curves show the best fits to the data using the LK formula [Eq. (2)]. The graph shows that the LK formula fits the data well. From the best-fit parameters, we extracted the effective masses to be $m^*_\chi = (0.18 \pm 0.01)m_o$, $m^*_\epsilon = (0.14 \pm 0.00)m_o$, $m^*_\phi = (0.28 \pm 0.01)m_o$, $m^*_\gamma = (0.28 \pm 0.01)m_o$, $m^*_\eta = (0.17 \pm 0.02)m_o$, and $m^*_\lambda = (0.59 \pm 0.05)m_o$, where m_o is the rest mass of an electron. These values are comparable with the effective masses of $YbTi_3Bi_4$ [36]. Note that m^*_λ is much higher than for the other frequencies, but high-frequency signals are reported to have high effective masses also in other kagome compounds [49–51]. The effective masses obtained from the DFT calculations using the SKEAF code were also compared with the experimentally determined values, as summarized in Table II.

TABLE II. Comparison between experimental effective masses (m^*) obtained from dHvA oscillations and DFT band effective masses (m^*_b).

Orbit	χ	ϵ	ϕ	γ	η	λ
Expt.	0.18	0.14	0.28	0.28	0.17	0.59
DFT	0.22	0.65	0.81	0.60	0.87	1.36

We performed Dingle temperature analyses for the two frequency components, F_χ and F_ϵ, as shown in Fig. 2(d). The scattered points represent the experimental data, while the dotted curves correspond to the best fits using the Lifshitz-Kosevich formula (2). From these fits, we extracted Dingle temperatures of $T_D = 4.8 \pm 0.8$ K for the χ orbit and $T_D = 35 \pm 5$ K for the ϵ orbit. Using these values, we further estimated the associated Fermi velocity, quantum scattering time, mean free path, and quantum mobility, which are summarized in Table III. The lower T_D of the χ orbit indicates weaker impurity or defect scattering, resulting in enhanced quasiparticle lifetime, longer mean free path, and higher mobility. In contrast, the considerably higher T_D of the ϵ orbit signifies stronger scattering, leading to a shorter lifetime, reduced mean free path, and lower mobility.

It is noted that the fit for the temperature dependence of the oscillation amplitude corresponding to F_χ is not as good as that for other frequencies such as F_ε. This deviation from the ideal LK behavior is likely due to interference effects from the neighboring frequencies F_β and F_δ, whose proximity in the FFT spectrum leads to partial overlap of the oscillation components. Such interference can affect the extracted amplitudes and may also influence the physical parameters derived from the Dingle analysis for F_χ in Table III.

To investigate the origin of the frequency peaks in Fig. 2 and determine the topology of the corresponding Fermi surfaces, we carried out torque measurements at different tilt angles. Figure 3(a) shows the torque data at selected θ values. As seen in the graph, the amplitude and period of the dHvA oscillations change with θ. More interestingly, the oscillations are suppressed at higher θ values and completely suppressed when the magnetic field is aligned along the surface (ab-plane) of the sample, even under high magnetic fields up to 41.5 T. For quantitative analysis, we extracted frequencies at each angle and present them in Fig. 3(b). F_χ is the dominant

TABLE III. Parameters obtained from the dHvA oscillations of $CaTi_3Bi_4$: frequency (F), Fermi wave vector (k_F), Fermi surface area (S_F), effective mass (m^*/m_0), Fermi velocity (v_F), Dingle temperature (T_D), quantum relaxation time (τ_s), mean free path (ℓ_{2D}), and quantum mobility (μ).

Orbit	F (T)	k_F (Å^{-1})	S_F (Å^{-2})	m^*/m_0	v_F (10^4 m/s)	T_D (K)	τ_s (10^{-13} s)	ℓ_{2D} (nm)	μ (cm^2/Vs)
χ	176	0.07	1.68	0.18	46.9	4.82	2.51	117.6	2446
ϵ	647	0.14	6.17	0.14	115.5	35.0	0.34	39.9	433

frequency and persists only up to 70°. The frequency peaks systematically shift to the right (higher values) as θ is increased. As expected, there is no frequency at $\theta = 90°$. The absence of quantum oscillations, and hence frequency signals, at $\theta = 90°$ strongly suggests that these frequencies originate from quasi-two-dimensional Fermi surfaces [52,53].

To better interpret the experimental observations, we performed first-principles DFT calculations to compute the electronic structure. Figure 4(a) shows the electronic bands of $CaTi_3Bi_4$ along a high-symmetry path (left inset) with and without including SOC. As seen in the figure, multiple bands cross the Fermi level, indicating metallic behavior, which is consistent with the electrical transport data (Fig. 1). Several notable features appear near the Fermi level, including a flat band (FB), a Dirac point (DP), and a van Hove singularity (VHS). Such features are expected in kagome materials [27–29,54,55] and can potentially be tuned closer to the Fermi energy through doping or external pressure. With the inclusion of SOC, the electronic bands exhibit the expected shifts due to the presence of heavy elements such as Bi. The density of states (DOS), shown in the right inset, reveals a nonzero DOS at E_F, further confirming the metallic character. Most importantly, the electronic states near the Fermi level originate primarily from Ti-d and Bi-p orbitals, with minimal contribution from Ca-s orbitals. Thus, the low-energy electronic properties are dominated by the kagome layer of Ti atoms. A similar dominance of kagome-layer contributions has been reported in other V- and Ti-based kagome compounds [28,51,56–58].

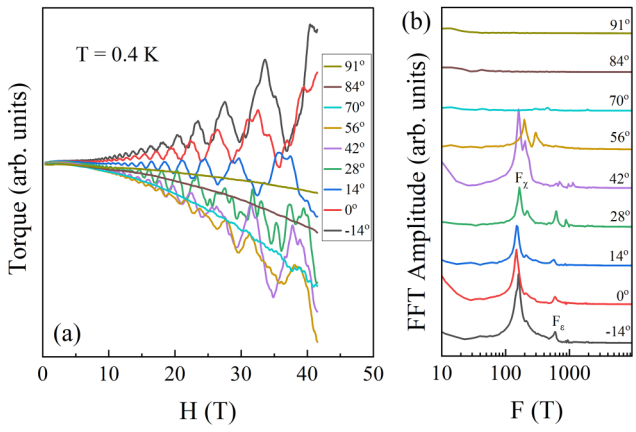

FIG. 3. (a) Angular dependence of magnetic torque in $CaTi_3Bi_4$, showing dHvA oscillations at various tilt angles θ. The oscillation amplitude varies with θ. (b) Corresponding frequency spectra from (a), where the peaks shift to higher frequencies as θ increases. The oscillations vanish above 70°, consistent with the absence of peaks in the FFT. Data at selected angles are shown for clarity, and the spectra are vertically offset for better visibility.

To examine the effect of pressure, we performed electronic band-structure calculations at 5 and 10 GPa. Figure 4(b) compares the band structures at 0, 5, and 10 GPa. A clear and systematic shift of the electronic states with increasing pressure is observed; in particular, the VHS at the Y point moves closer to the Fermi level, as highlighted by the dashed arrow. We previously conducted pressure-dependent studies [55,59] in the 135-kagome family (CsV_3Sb_5), where we found a similar pressure-induced evolution of the electronic structure. We also performed a chemical-pressure study [46,59,60] by substituting V with Ti. Because Ti is smaller than V and lies to the left in the periodic table, this substitution effectively introduces both hole doping and chemical pressure. In that system, we observed an enhancement of T_c, suppression of the CDW phase, and shifts in key electronic features similar to those found in $CaTi_3Bi_4$. Together, these observations demonstrate that external or chemical pressure is an effective means of tuning the electronic structure in kagome materials.

Five electronic bands (104, 105, 106, 107, and 108) cross the Fermi level and contribute to the Fermi surface of $CaTi_3Bi_4$. The contributions from each band are shown in Fig. 5. The calculated Fermi surface consists of multiple concentric cylindrical sheets at the Brillouin zone corners, along with a large central sheet centered at the Γ point. Two smaller, concavelike features also appear at the top and bottom of the zone. The presence of cylindrical Fermi surfaces is consistent with the nearly $1/\cos\theta$ behavior of the frequencies observed in the dHvA oscillations, as discussed in Fig. 6. The Fermi surface of $CaTi_3Bi_4$ is consistent with that of the isostructural compound $YbTi_3Bi_4$ and resembles those found in other V-based kagome systems, such as AV_3Sb_5 (A = Cs, K, Rb) and the Ti-based $CsTi_3Bi_5$ [56,57].

To quantitatively compare with experiment, we computed the theoretical dHvA frequencies by evaluating the extremal cross-sectional areas of the Fermi surfaces using the SKEAF code [43]. According to Onsager's relation [47,59,61], the quantum oscillation frequency F is directly proportional to the extremal cross-sectional area A, $F = \frac{\hbar}{2\pi e}A$. Figure 6 compares the experimental dHvA frequencies with the DFT-derived values from the Fermi surface of each band. As seen in the graph, the theoretical and experimental values are in good agreement, confirming the reliability of our interpretation. Furthermore, all the dHvA frequencies, except the 13 T branch, nearly follow the expected $F(\theta) = F(0)/\cos\theta$ dependence, characteristic of a cylindrical Fermi surface and consistent with the calculated Fermi surface (Fig. 5).

The effective masses obtained from the DFT calculations using the SKEAF code were also compared with the experimentally determined values, as summarized in Table II. The calculated masses are generally higher, in some cases nearly twice the experimental ones. Such discrepancies are typical in

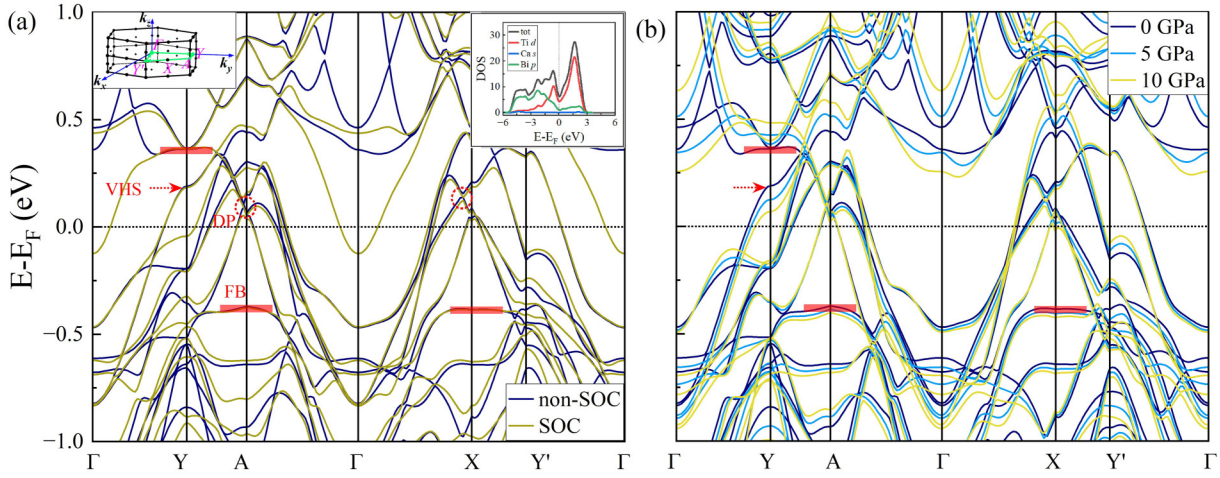

FIG. 4. (a) Electronic band structure of $CaTi_3Bi_4$ with and without SOC along the high-symmetry k-path shown in the left inset. Several key features appear near the Fermi level, including a Dirac point (DP), a flat band (FB), and a van Hove singularity (VHS), marked by dotted circles, shaded regions, and dashed arrows, respectively. Noticeable changes occur in the bands near the Fermi level when SOC is included. Right inset: Partial density of states (DOS) for $CaTi_3Bi_4$. The total DOS near E_F is dominated by Ti-d and Bi-p orbitals, with little or no contribution from the Ca-s orbital. (b) Electronic band structures at three different pressures (0, 5, and 10 GPa). Pressure induces a clear shift in the bands; in particular, the VHS at the Y point moves closer to the Fermi level, as indicated by the dashed arrow. Dashed lines indicate the Fermi level.

metallic systems where DFT tends to overestimate the band curvature due to the absence of many-body renormalization effects. The smaller experimental masses indicate that electron correlation effects are weak in this compound, consistent with its simple metallic nature.

IV. SUMMARY

In summary, we investigated the Ti-based kagome compound $CaTi_3Bi_4$ through single-crystal growth, bulk characterization, high-field quantum oscillation measurements, and first-principles calculations. Electrical transport measurements reveal metallic behavior with a RRR of 12, while magnetic susceptibility, specific heat, and resistivity confirm the absence of a magnetic ground state. The torque signal measured up to 41.5 T exhibits well-defined dHvA oscillations with nine distinct frequencies ranging from ∼13 to 6164 T. These frequency components display an angular dependence close to $1/\cos\theta$ (θ being the tilt angle of the magnetic field), consistent with the presence of quasi-two-dimensional cylindrical Fermi sheets in this material. The temperature and field dependence of the dHvA oscillations were analyzed using the Lifshitz-Kosevich theory, and the

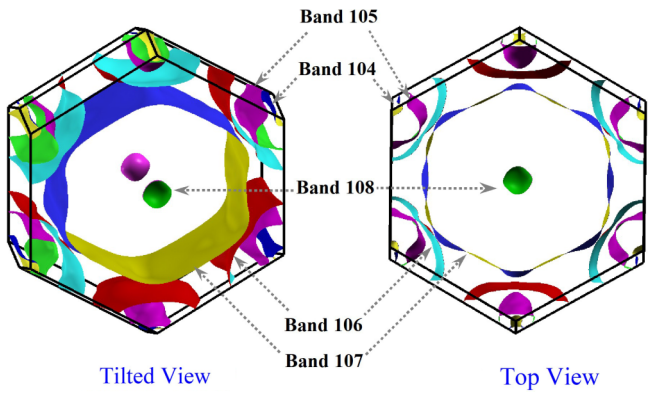

FIG. 5. Tilted and top views of the Fermi surface of $CaTi_3Bi_4$. Five bands (104, 105, 106, 107, and 108) cross the Fermi level, forming the Fermi surface. Three cylindrical pockets appear at the corners of the Brillouin zone, while a large pocket is centered at the Γ point.

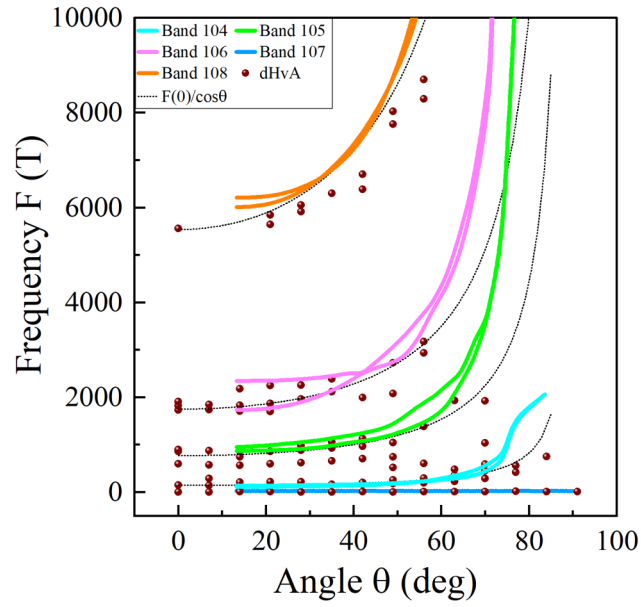

FIG. 6. Comparison of DFT-calculated quantum oscillation frequencies with experimental dHvA data for $CaTi_3Bi_4$. Solid circles represent theoretical frequencies from each band, while open circles correspond to experimental values, showing good agreement. Most frequencies follow an approximately $1/\cos\theta$ behavior, indicated by the dashed curves, suggesting they originate from cylindrical Fermi surfaces.

resulting physical parameters characterizing the Fermi surface are summarized in Table III.

To support these experimental observations, we performed first-principles calculations based on DFT. The calculations reveal several features, including Dirac-like dispersions, van Hove singularities, and flat bands. With the inclusion of SOC, the electronic bands shift and exhibit splittings near the Fermi level; however, the overall electronic structure and Fermi-surface topology remain qualitatively similar. To explore the tunability of the electronic structure, we performed pressure-dependent DFT calculations at 0, 5, and 10 GPa. All characteristic features–the Dirac point, flat bands, and van Hove singularities—exhibit noticeable shifts under applied pressure. Notably, the van Hove singularity at the Y point moves closer to the Fermi level, suggesting that hydrostatic pressure may drive $CaTi_3Bi_4$ toward a regime where collective or correlated behavior could emerge. While lattice-dynamics calculations would offer additional insight into possible structural or dynamical instabilities, they require large supercells and are computationally not feasible at the moment. A detailed phonon study, particularly under pressure, is therefore left for future work. The computed Fermi surface, consisting of a central cylindrical sheet and half-cylinder–like pockets at the Brillouin zone corners, yields extremal cross sections in good agreement with the experimental frequencies, both in magnitude and angular dependence. This correspondence indicates that DFT accurately captures the Fermi surface topology with negligible many-body renormalization in $CaTi_3Bi_4$.

It is worth noting that, unlike the vanadium-based kagome family AV_3Sb_5, which exhibits multiple collective quantum phenomena such as charge-density-wave order and superconductivity, the Fermi surface topology in those systems could not be uniquely resolved from quantum oscillation measurements due to the presence of several overlapping frequency components. In contrast, the kagome compound $CaTi_3Bi_4$, while not showing such emergent quantum states, exhibits well-resolved de Haas–van Alphen oscillations whose frequencies match precisely with those predicted by DFT calculations. This clear correspondence provides a rare example within the kagome family where the experimentally observed and theoretically predicted Fermi surfaces can be directly compared. Therefore, $CaTi_3Bi_4$ serves as a model system for understanding the intrinsic electronic structure of kagome metals without the complications arising from competing quantum orders.

ACKNOWLEDGMENTS

This work was supported in part by the U.S. Department of Energy, Office of Science, Office of Workforce Development for Teachers and Scientists (WDTS) under the Visiting Faculty Program (VFP) at Los Alamos National Laboratory, administered by the Oak Ridge Institute for Science and Education. The work at West Texas A&M University (WTAMU) is supported by the Killgore Undergraduate and Graduate Student Research Grants, the Welch Foundation (Grant No. AE-0025) and the National Science Foundation (Award No. 2336011). The computations were performed on the WTAMU HPC cluster, which was funded by the National Science Foundation (NSF CC* GROWTH 2018841). Work by B.R.O. is supported by the U.S. Department of Energy (DOE), Office of Science, Basic Energy Sciences (BES), Materials Sciences and Engineering Division. A portion of this work was performed at the National High Magnetic Field Laboratory, which is supported by National Science Foundation Cooperative Agreement No. DMR-2128556 and the State of Florida.

DATA AVAILABILITY

The data that support the findings of this article are not publicly available. The data are available from the authors upon reasonable request.

[1] L. Ye, M. Kang, J. Liu, F. von Cube, C. R. Wicker, T. Suzuki, C. Jozwiak, A. Bostwick, E. Rotenberg, D. C. Bell, L. Fu, R. Comin, and J. G. Checkelsky, Massive Dirac fermions in a ferromagnetic kagome metal, Nature (London) **555**, 638 (2018).

[2] J.-X. Yin, W. Ma, T. A. Cochran, X. Xu, S. S. Zhang, H.-J. Tien, N. Shumiya, G. Cheng, K. Jiang, B. Lian, *et al.*, Quantum-limit Chern topological magnetism in $TbMn_6Sn_6$, Nature (London) **583**, 533 (2020).

[3] K. Jiang, T. Wu, J.-X. Yin, Z. Wang, M. Z. Hasan, S. D. Wilson, X. Chen, and J. Hu, Kagome superconductors AV_3Sb_5 ($A = K$, Rb, Cs), Natl. Sci. Rev. **10**, nwac199 (2022).

[4] M. Mekata, Kagome: The story of the basketweave lattice, Phys. Today **56**(2), 12 (2003).

[5] B. R. Ortiz, L. C. Gomes, J. R. Morey, M. Winiarski, M. Bordelon, J. S. Mangum, I. W. H. Oswald, J. A. Rodriguez-Rivera, J. R. Neilson, S. D. Wilson, E. Ertekin, T. M. McQueen, and E. S. Toberer, New kagome prototype materials: Discovery of KV_3Sb_5, RbV_3Sb_5, and CsV_3Sb_5, Phys. Rev. Mater. **3**, 094407 (2019).

[6] K. Shtefiienko, C. Phillips, M. J. Stitz, G. Pokharel, S. D. Wilson, D. E. Graf, and K. Shrestha, Pressure effects on the Fermi surface of Ti-doped CsV_3Sb_5, Phys. Rev. B **111**, 235135 (2025).

[7] B. R. Ortiz, S. M. Teicher, Y. Hu, J. L. Zuo, P. M. Sarte, E. C. Schueller, A. M. Abeykoon, M. J. Krogstad, S. Rosenkranz, R. Osborn, *et al.*, CsV_3Sb_5: A $\mathbb{Z}_2$ topological kagome metal with a superconducting ground state, Phys. Rev. Lett. **125**, 247002 (2020).

[8] F. H. Yu, D. H. Ma, W. Z. Zhuo, S. Q. Liu, X. K. Wen, B. Lei, J. J. Ying, and X. H. Chen, Unusual competition of superconductivity and charge-density-wave state in a compressed topological kagome metal, Nat. Commun. **12**, 3645 (2021).

[9] K. Y. Chen, N. N. Wang, Q. W. Yin, Y. H. Gu, K. Jiang, Z. J. Tu, C. S. Gong, Y. Uwatoko, J. P. Sun, H. C. Lei, J. P. Hu, and J. G. Cheng, Double superconducting dome and triple enhancement of T_c in the kagome superconductor CsV_3Sb_5 under high pressure, Phys. Rev. Lett. **126**, 247001 (2021).

[10] N. N. Wang, K. Y. Chen, Q. W. Yin, Y. N. N. Ma, B. Y. Pan, X. Yang, X. Y. Ji, S. L. Wu, P. F. Shan, S. X. Xu, Z. J. Tu, C. S. Gong, G. T. Liu, G. Li, Y. Uwatoko, X. L. Dong, H. C. Lei, J. P. Sun, and J.-G. Cheng, Competition between charge-density-wave and superconductivity in the kagome metal RbV_3Sb_5, Phys. Rev. Res. **3**, 043018 (2021).

[11] M. Kang, S. Fang, J.-K. Kim, B. R. Ortiz, S. H. Ryu, J. Kim, J. Yoo, G. Sangiovanni, D. D. Sante, B.-G. Park, C. Jozwiak, A. Bostwick, E. Rotenberg, E. Kaxiras, S. D. Wilson, J.-H. Park, and R. Comin, Massive Dirac fermions in a ferromagnetic kagome metal, Nat. Phys. **18**, 301 (2022).

[12] S. D. Wilson and B. R. Ortiz, AV_3Sb_5 kagome superconductors, Nat. Rev. Mater. **9**, 420 (2024).

[13] B. R. Ortiz, P. M. Sarte, E. M. Kenney, M. J. Graf, S. M. L. Teicher, R. Seshadri, and S. D. Wilson, Superconductivity in the $\mathbb{Z}_2$ kagome metal KV_3Sb_5, Phys. Rev. Mater. **5**, 034801 (2021).

[14] F. H. Yu, T. Wu, Z. Y. Wang, B. Lei, W. Z. Zhuo, J. J. Ying, and X. H. Chen, Concurrence of anomalous Hall effect and charge density wave in a superconducting topological kagome metal, Phys. Rev. B **104**, L041103 (2021).

[15] Q. Yin, Z. Tu, C. Gong, Y. Fu, S. Yan, and H. Lei, Superconductivity and normal-state properties of kagome metal RbV_3Sb_5 single crystals, Chin. Phys. Lett. **38**, 037403 (2021).

[16] S.-Y. Yang, Y. Wang, B. R. Ortiz, D. Liu, J. Gayles, E. Derunova, R. Gonzalez-Hernandez, L. Šmejkal, Y. Chen, S. S. P. Parkin, S. D. Wilson, E. S. Toberer, and T. M. M. N. Ali, Giant, unconventional anomalous Hall effect in the metallic frustrated magnet candidate, KV_3Sb_5, Sci. Adv. **6** (2020).

[17] K. Nakayama, Yongkai, T. Kato, M. Liu, Z. Wang, T. Takahashi, Y. Yao, and T. Sato, Carrier injection and manipulation of charge-density wave in kagome superconductor CsV_3Sb_5, Phys. Rev. X **12**, 011001 (2022).

[18] B. R. Ortiz, S. M. L. Teicher, L. Kautzsch, P. M. Sarte, N. Ratcliff, J. Harter, J. P. C. Ruff, R. Seshadri, and S. D. Wilson, Fermi surface mapping and the nature of charge-density-wave order in the kagome superconductor CsV_3Sb_5, Phys. Rev. X **11**, 041030 (2021).

[19] H. Luo, Q. Gao, H. Liu, Y. Gu, D. Wu, C. Yi, J. Jia, S. Wu, X. Luo, Y. Xu, *et al.*, Electronic nature of charge density wave and electron-phonon coupling in kagome superconductor KV_3Sb_5, Nat. Commun. **13**, 273 (2022).

[20] Y. Fu, N. Zhao, Z. Chen, Q. Yin, Z. Tu, C. Gong, C. Xi, X. Zhu, Y. Sun, K. Liu, and H. Lei, Quantum transport evidence of topological band structures of kagome superconductor CsV_3Sb_5, Phys. Rev. Lett. **127**, 207002 (2021).

[21] W. Zhang, L. Wang, C. W. Tsang, X. Liu, J. Xie, W. C. Yu, K. T. Lai, and S. K. Goh, Emergence of large quantum oscillation frequencies in thin flakes of the kagome superconductor CsV_3Sb_5, Phys. Rev. B **106**, 195103 (2022).

[22] C. Broyles, D. Graf, H. Yang, X. Dong, H. Gao, and S. Ran, Effect of the interlayer ordering on the Fermi surface of kagome superconductor CsV_3Sb_5 revealed by quantum oscillations, Phys. Rev. Lett. **129**, 157001 (2022).

[23] K. Shrestha, M. Shi, T. Nguyen, D. Miertschin, K. Fan, L. Deng, D. E. Graf, X. Chen, and C.-W. Chu, Fermi surface mapping of the kagome superconductor RbV_3Sb_5 using de Haas–van Alphen oscillations, Phys. Rev. B **107**, 075120 (2023).

[24] K. Shrestha, R. Chapai, B. K. Pokharel, D. Miertschin, T. Nguyen, X. Zhou, D. Y. Chung, M. G. Kanatzidis, J. F. Mitchell, U. Welp, D. Popović, D. E. Graf, B. Lorenz, and W. K. Kwok, Nontrivial Fermi surface topology of the kagome superconductor CsV_3Sb_5 probed by de Haas–van Alphen oscillations, Phys. Rev. B **105**, 024508 (2022).

[25] B. R. Ortiz, H. Miao, D. S. Parker, F. Yang, G. D. Samolyuk, E. M. Clements, A. Rajapitamahuni, T. Yilmaz, E. Vescovo, J. Yan, *et al.*, Evolution of highly anisotropic magnetism in the titanium-based kagome metals $LnTi_3Bi_4$ (Ln: $La\cdots Gd^{3+}$, Eu^{2+}, Yb^{2+}), Chem. Mater. **35**, 9756 (2023).

[26] B. R. Ortiz, H. Zhang, K. Górnicka, D. S. Parker, G. D. Samolyuk, F. Yang, H. Miao, Q. Lu, R. G. Moore, A. F. May, *et al.*, Intricate magnetic landscape in antiferromagnetic kagome metal $TbTi_3Bi_4$ and interplay with $Ln_{2-x}Ti_{6+x}Bi_9$(Ln : Tb $\cdots$ Lu) Shurikagome metals, Chem. Mater. **36**, 8002 (2024).

[27] M. I. Mondal, A. P. Sakhya, M. Sprague, B. R. Ortiz, M. Matzelle, B. Ghosh, N. Valadez, I. B. Elius, A. Bansil, and M. Neupane, Observation of multiple flat bands and Van Hove singularities in the distorted kagome metal $NdTi_3Bi_4$, Phys. Rev. B **112**, L121104 (2025).

[28] A. P. Sakhya, B. R. Ortiz, B. Ghosh, M. Sprague, M. I. Mondal, M. Matzelle, I. Bin Elius, N. Valadez, D. G. Mandrus, A. Bansil, *et al.*, Diverse electronic landscape of the kagome metal $YbTi_3Bi_4$, Commun. Mater. **5**, 241 (2024).

[29] Y. Hu, C. Le, L. Chen, H. Deng, Y. Zhou, N. C. Plumb, M. Radovic, R. Thomale, A. P. Schnyder, J.-X. Yin, G. Wang, X. Wu, and M. Shi, Magnetic coupled electronic landscape in bilayer-distorted titanium-based kagome metals, Phys. Rev. B **110**, L121114 (2024).

[30] Z. Jiang, T. Li, J. Yuan, Z. Liu, Z. Cao, S. Cho, M. Shu, Y. Yang, J. Ding, Z. Li, *et al.*, Direct observation of topological surface states in the layered kagome lattice with broken time-reversal symmetry, arXiv:2309.01579.

[31] E. Cheng, K. Wang, Y. Hao, W. Chen, H. Tan, Z. Li, M. Wang, W. Gao, D. Wu, *et al.*, Interwoven magnetic kagome metal overcomes geometric frustration, Nat. Mater. (2025).

[32] Z. Zheng, L. Chen, X. Ji, Y. Zhou, G. Qu, M. Hu, Y. Huang, H. Weng, T. Qian, and G. Wang, Anisotropic magnetism and band evolution induced by ferromagnetic phase transition in titanium-based kagome ferromagnet $SmTi_3Bi_4$, Sci. Chin. Phys. Mech. Astron. **67**, 267411 (2024).

[33] J. Guo, L. Zhou, J. Ding, G. Qu, Z. Liu, Y. Du, H. Zhang, J. Li, Y. Zhang, F. Zhou, *et al.*, Tunable magnetism and band structure in kagome materials $RETi_3Bi_4$ family with weak interlayer interactions, Sci. Bull. **69**, 2660 (2024).

[34] L. Chen, Y. Zhou, H. Zhang, X. Ji, K. Liao, Y. Ji, Y. Li, Z. Guo, X. Shen, R. Yu, *et al.*, Tunable magnetism in titanium-based kagome metals by rare-earth engineering and high pressure, Commun. Mater. **5**, 73 (2024).

[35] P. Park, B. R. Ortiz, M. Sprague, A. P. Sakhya, S. A. Chen, M. D. Frontzek, W. Tian, R. Sibille, D. G. Mazzone, C. Tabata, *et al.*, Spin density wave and van Hove singularity in the kagome metal $CeTi_3Bi_4$, Nat. Commun. **16**, 4384 (2025).

[36] K. Shtefiienko, C. Phillips, B. R. Ortiz, D. E. Graf, and K. Shrestha, Electronic structure of the kagome metal $YbTi_3Bi_4$ studied using torque magnetometry, Phys. Rev. B **111**, 035145 (2025).

[37] A. Ovchinnikov and S. Bobev, Bismuth As a reactive solvent in the synthesis of multicomponent transition-metal-bearing bismuthides, Inorg. Chem. **59**, 3459 (2020).

[38] P. C. Canfield, T. Kong, U. S. Kaluarachchi, and N. H. Jo, Use of frit-disc crucibles for routine and exploratory solution growth of single crystalline samples, Philos. Mag. **96**, 84 (2016).

[39] P. Giannozzi, S. Baroni, N. Bonini, M. Calandra, R. Car, C. Cavazzoni, D. Ceresoli, G. L. Chiarotti, M. Cococcioni, I. Dabo, *et al.*, QUANTUM ESPRESSO: A modular and open-source software project for quantumsimulations of materials, J. Phys.: Condens. Matter **21**, 395502 (2009).

[40] W. Kohn and L. J. Sham, Self-consistent equations including exchange and correlation effects, Phys. Rev. **140**, A1133 (1965).

[41] P. Hohenberg and W. Kohn, Inhomogeneous electron gas, Phys. Rev. **136**, B864 (1964).

[42] J. P. Perdew, A. Ruzsinszky, G. I. Csonka, O. A. Vydrov, G. E. Scuseria, L. A. Constantin, X. Zhou, and K. Burke, Restoring the density-gradient expansion for exchange in solids and surfaces, Phys. Rev. Lett. **100**, 136406 (2008).

[43] P. M. C. Rourke and S. Julian, Numerical extraction of de Haas–van Alphen frequencies from calculated band energies, Comput. Phys. Commun. **183**, 324 (2012).

[44] C. Kittel and P. McEuen, *Introduction to Solid State Physics* (John Wiley & Sons, New York, 2018).

[45] N. W. Ashcroft and N. Mermin, *Solid State Physics* (Holt, Rinehart and Winston, New York, 1976), Appendix C .

[46] K. Shtefiienko, S. Zhang, U. A. de la Sierra, G. Pokharel, and K. Shrestha, Superconducting properties of the Ti-doped KV_3Sb_5 kagome compound, Phys. Rev. B **112**, 115140 (2025).

[47] D. Shoenberg, *Magnetic Oscillations in Metals* (Cambridge University Press, Cambridge, UK, 1984).

[48] K. Shrestha, V. Marinova, B. Lorenz, and P. C. Chu, Shubnikov–de Haas oscillations from topological surface states of metallic $Bi_2Se_{2.1}Te_{0.9}$, Phys. Rev. B **90**, 241111(R) (2014).

[49] G. Zheng, Y. Zhu, S. Mozaffari, N. Mao, K.-W. Chen, K. Jenkins, D. Zhang, A. Chan, H. W. S. Arachchige, R. P. Madhogaria, *et al.*, Quantum oscillations evidence for topological bands in kagome metal ScV_6Sn_6, J. Phys.: Condens. Matter **36**, 215501 (2024).

[50] Z. Rehfuss, C. Broyles, D. Graf, Y. Li, H. Tan, Z. Zhao, J. Liu, Y. Zhang, X. Dong, H. Yang, H. Gao, B. Yan, and S. Ran, Quantum oscillations in kagome metals $CsTi_3Bi_5$ and $RbTi_3Bi_5$, Phys. Rev. Mater. **8**, 024003 (2024).

[51] K. Shrestha, B. Regmi, G. Pokharel, S.-G. Kim, S. D. Wilson, D. E. Graf, B. A. Magar, C. Phillips, and T. Nguyen, Electronic properties of kagome metal ScV_6Sn_6 using high-field torque magnetometry, Phys. Rev. B **108**, 245119 (2023).

[52] Y. Ando, Topological insulator materials, J. Phys. Soc. Jpn. **82**, 102001 (2013).

[53] A. A. Taskin and Y. Ando, Berry phase of nonideal Dirac fermions in topological insulators, Phys. Rev. B **84**, 035301 (2011).

[54] S. R. Bhandari, M. Zeeshan, V. Gusain, K. Shrestha, and D. Rai, First-principles study of the electronic structure, $\mathbb{Z}_2$ invariant, and quantum oscillation in the kagome material CsV_3Sb_5, APL Quantum **1**, 046118 (2024).

[55] S. R. Bhandari, V. Gusain, M. Zeeshan, D. Rai, and K. Shrestha, Pressure effects on the electronic structure of the kagome metal, APL Quantum **2**, 016133 (2025).

[56] K. Shrestha, M. Shi, B. Regmi, T. Nguyen, D. Miertschin, K. Fan, L. Z. Deng, N. Aryal, S.-G. Kim, D. E. Graf, *et al.*, High quantum oscillation frequencies and nontrivial topology in kagome superconductor KV_3Sb_5 probed by torque magnetometry up to 45 T, Phys. Rev. B **107**, 155128 (2023).

[57] J. Yang, X. Yi, Z. Zhao, Y. Xie, T. Miao, H. Luo, H. Chen, B. Liang, W. Zhu, Y. Ye, *et al.*, Observation of flat band, dirac nodal lines and topological surface states in kagome superconductor $CsTi_3Bi_5$, Nat. Commun. **14**, 4089 (2023).

[58] K. Shtefiienko, C. Phillips, S. Mozaffari, R. P. Madhogaria, W. R. Meier, D. G. Mandrus, D. E. Graf, and K. Shrestha, Electronic structure of YV_6Sn_6 probed by de Haasvan Alphen oscillations and density functional theory, APL Quantum **2**, 016118 (2025).

[59] C. Phillips, K. Shtefiienko, T. Nguyen, A. N. Capa Salinas, B. A. Magar, G. Pokharel, S. D. Wilson, D. E. Graf, and K. Shrestha, Fermi surface reconstruction under pressure in the kagome metal CsV_3Sb_5, Phys. Rev. B **110**, 205135 (2024).

[60] K. Shtefiienko, T. Beekmann, M. J. Stitz, G. Pokharel, S. D. Wilson, C. A. Mizzi, D. E. Graf, and K. Shrestha, De Haas–van Alphen effect in the Ti-doped CsV_3Sb_5 kagome compound under magnetic fields up to 41 Tesla, Phys. Rev. B **113**, 035119 (2026).

[61] T. Nguyen, N. Aryal, B. K. Pokharel, L. Harnagea, D. Mierstchin, D. Popović, D. E. Graf, and K. Shrestha, Fermiology of the Dirac type-II semimetal candidates (Ni, Zr)Te_2 using de Haas–van Alphen oscillations, Phys. Rev. B **106**, 075154 (2022).